Internal Waves Observations from the Surface Water Ocean Topography Mission: Combined sea surface height and roughness measurements

V. Cheshm Siyahi[1], V. Kudryavtsev [1,2], B. Chapron[3], and F. Collard[4]

[1]Satellite Oceanography Laboratory, Russian State Hydrometeorological University, Saint Petersburg, 192007, Russian Federation
[2]Marine Hydrophysical Institute RAS, Sevastopol, 299011, Russian Federation
[3]Univ. Brest, CNRS, IRD, Ifremer, Laboratoire d'Océanographie Physique et Spatiale (LOPS), IUEM, Brest, 29280, France
[4]OceanDataLab, Locmaria-Plouzané, 29280, France

Key Points:

- Off the Amazon shelf SWOT data capture IWs signatures, showing joint SSH and NRCS anomaly variations corresponding to pycnocline displacements reaching up to 100 m
- Coincident NRCS and SSHA SWOT measurements help assess and refine the Modulation Transfer Function (MTF).
- MTF dependencies on IW wavelength, phase velocity, wind speed and direction, are quantified and interpreted using a radar imaging model (RIM).

Corresponding author: Bertrand Chapron, `Bertrand.Chapron@ifremer.fr`

Abstract

Observations of strong internal waves (IWs) off the Amazon Shelf by the Surface Water and Ocean Topography (SWOT) mission are analyzed. Distinct IWs signatures with wavelengths ranging from 3 to 50 km in coincident sea surface height anomalies (SSHA) and near-nadir normalized radar cross section (NRCS) are clearly identified. Using a three-layer approximation to describe the upper ocean stratification, SWOT SSHAs are converted to IW-induced thermocline displacements, reaching up to 80 m amplitude. This confirms SWOT's unique ability to quantitatively inform about the state of the ocean interior, the energy and depth distribution of IWs. Moreover, joint SWOT measurements of SSHAs and NRCS further provide new means to precisely study the mechanisms leading to identify IWs from radar intensity measurements. SWOT data can indeed be analyzed in terms of a modulation transfer function (MTF), relating the SWOT NRCS contrasts to divergence of IW surface currents derived from SWOT SSHA measurements. Thanks to these new observations, SWOT-based MTF estimates are derived to quantify relationships between the NRCS contrasts, the amplitude and wavenumber of IWs, and the local wind conditions. In particular, it is shown that the maximum SWOT NRCS contrasts occur when IWs propagate in the wind direction, corresponding to resonant conditions between short wind waves and internal waves.

Plain Language Summary

SWOT observations are shedding new lights on internal wave (IW) dynamics with coincident sea surface height and roughness modulations responding to the passage of IWs. Traveling IWs strongly impact inner layers of the upper ocean, with localized intense vertical motions shifting the boundary between warm and cold water by up to 100 meters. SWOT high resolution sea surface height measurements help clearly identify IWs with wavelengths from about 3 to 50 kilometers. These measurements, combined with radar intensity signals, open new means to quantify sea surface roughness hydrodynamical modulations. The strongest signatures are confirmed to occur under weak wind conditions and when IWs travel along the wind direction. Overall, SWOT combined observations quantify the upper ocean's inner dynamics, and can help quantifying IWs effects, which is valuable for various applications.

1 Introduction

Internal waves (IWs) are increasingly recognized as critical contributors to global mixing in the upper ocean layers. This mixing process significantly impacts the near-surface temperature structure, air-sea exchange, and ultimately the evolution of the climate system (Shroyer et al., 2010). These waves arise within the stratified ocean, where less dense water overlies denser water. Perturbations from external forces, such as interactions of surface tides with underwater topographical features, can trigger the generation of IWs at isopycnals (New, 1988). As large-scale internal tides (ITs) travel away from topographical obstacles, they steepen and break down into shorter-period, nonlinear IWs that remain synchronized with the ITs (Pingree et al., 1986; Gerkema, 1996; Shaw et al., 2009). Breaking, these IWs are believed to play a major role in near-surface mixing through the constant generation of instabilities as they propagate (Moum et al., 2003).

Although high resolution satellite sensors, such as optical, synthetic aperture radars (SAR), and altimeters, have long been instrumental in identifying IWs (Li et al., 2008, 2013; Dong et al., 2016; M. Zhang et al., 2019; Xudong et al., 2020; Kudryavtsev et al., 2005, 2012; Jackson, 2007; de Macedo et al., 2023; J. M. Magalhães et al., 2016; J. M. Magalhães & Da Silva, 2018), only limited information on IWs could be quantitatively retrieved. The recently launched Surface Water and Ocean Topography (SWOT) mission promises a significant leap forward in the observation of IWs compared to previous satellite observations (Fu et al., 2024; Morrow et al., 2019). SWOT's Ka-band radar interferometer (KaRIn) observations make it possible to capture the detailed patterns of IWs, including wave groups and leading edges (Fu et al., 2024; Morrow et al., 2019). But unlike past satellite observations that solely relied on surface roughness signatures from SAR or sunglint data from optical observations (Jackson, 2007; J. Magalhães et al., 2021; Kudryavtsev et al., 2005, 2012), SWOT provides a unique combination of SAR surface roughness images and elevation maps. This combined capability thus offers new means to more quantitatively access IW properties.

SWOT's advanced radar altimetry has already been demonstrated to excel in detecting IW-induced sea surface height anomalies (SSHA) with remarkable precision, capturing signals in the range of 10–20 cm (H. Zhang et al., 2024; X. Zhang & Li, 2024). Some investigations off Central California (Cai et al., 2024), showed how SWOT data complement in-situ measurements, revealing distinct modal compositions and energy flux variations driven by seasonal stratification and eddy dynamics, improving the accuracy of internal tidal corrections in altimetry. Qiu et al. (2024) used SWOT observations in the Indonesian seas to characterize IWs, generated through tide-topography interactions. They showed IWs exhibit seasonal and fortnightly variability influenced by upper-ocean stratification. In the Amazon shelf region, SWOT data has also been used to analyze ITs with unprecedented details, capturing high-resolution sea level anomalies to identify tidal signals (Tchilibou et al., 2024). Techniques such as harmonic and principal component analysis enable the separation of coherent and incoherent IT modes, shedding light on the role of stratification and background currents in modulating IT variability (Tchilibou et al., 2024). These studies collectively highlight SWOT's transformative role in the detection and analysis of IWs, significantly enhancing our understanding of their spatial and temporal variability across diverse marine environments.

Hereafter, we provide a detailed analysis of IWs off the Amazon shelf, utilizing high-resolution SWOT data to reconstruct IW parameters to examine and quantitatively characterize the modulation of SWOT normalized radar cross-section (NRCS) by IWs. Section 2 introduces the study area and datasets used in the analysis. Section 3 focuses on the reconstruction of IW parameters and pycnocline oscillations within the framework of a three-layer approximation model for stratified fluids. Section 4 provide a joint SWOT SSHA-NRCS data analysis, to develop a modulation transfer function (MTF) that links the NRCS and SSHA under varying wind conditions. Finally, Section 5 summarizes the main findings. A detailed description of the dispersion relation and vertical velocity profiles of IWs is provided in Appendix A.

2 Area and Data

2.1 Off the Amazon Shelf

The Amazon shelf is a breeding ground for powerful IWs. This area has been recognized by multiple studies (Brandt et al., 2002; J. M. Magalhães et al., 2016; Lentini et al., 2016; Bai et al., 2021; Tchilibou et al., 2022, 2024) for its intense generation of these waves. The dynamic nature of the Amazon shelf, influenced by the confluence of river discharge, tidal forces, and ocean currents, creates a conducive environment for IW formation. Several researchers have documented IWs traveling in two main directions: offshore (Brandt et al., 2002; J. M. Magalhães et al., 2016) and along the shelf (Lentini et al., 2016; Bai et al., 2021). Offshore IWs are linked to areas with strong internal tides near steep slopes on the Amazon shelf (J. M. Magalhães et al., 2016), where the 1-day SWOT observation captured them.

The offshore-propagating IWs are particularly notable due to their association with the steep topographical features of the shelf (J. M. Magalhães et al., 2016). These waves are generated as tidal forces interact with the abrupt underwater slopes, converting tidal energy into IW energy (Brandt et al., 2002; J. M. Magalhães et al., 2016). These IWs can extend far into the open ocean, carrying energy and momentum away from the shelf (Bai et al., 2021). In contrast, the IWs traveling along the shelf are primarily influenced by the along-shelf currents and the bathymetric variations parallel to the coast.

Recent SWOT satellite mission, have provided new insights into the spatial and temporal characteristics of IWs on the Amazon shelf. The SWOT observations have enabled researchers to capture high-resolution images of IW patterns, shedding light on their generation mechanisms, propagation pathways, and interaction with other oceanographic features. These findings are crucial for improving our understanding of the role of IWs in coastal dynamics and their potential impact on climate and marine ecosystems (Fu et al., 2024; Tchilibou et al., 2024).

2.2 SWOT SSH

In this study the Low Resolution (LR) "Unsmoothed" SWOT product (SWOT Project, 2023), from the KaRIn observations, with spatial resolution of approximately abut 250 m are used. The level 2 (L2) products include SSH, NRCS, and mean sea surface height (MSSH) above the reference ellipsoid from CNES/CLS model for 2015 year. Recently released level 3 (L3) "Unsmoothed" data include products, such as SSHA, NRCS, MSSH, geostrophic current, with spatial resolution of about 250 m.

To obtain SSHA from the SSH L2 product, we subtract the mean SSH (MSSH), also available at L2 datasets. The difference between SSH and MSSH represent the SSHA signals considered here. Fields of SSHA in the Amazon area is shown in Figures 1a and 1c. Referring to these cases, a systematic cross-track trend appears which is caused by roll/phase errors. Roll/phase errors in KaRIn occur due to slight tilts of the spacecraft and timing mismatches in the radar system. These errors result in a consistent slope across the instrument's swath, distorting the measured height of the Earth's surface. The cross-track trend obtained by averaging the SSH along the azimuth, which are shown in inserted graph of Figure 1e and Figure 1f. The cross-track trend is then removed from the data. Next, we applied a low-pass filter to remove along-track variations with wavelengths larger than 200 km. The remaining part, illustrated on Figures 1b and 1d, is considered to be "corrected" SWOT KaRIn wide-swath observation of SSHA, h, showing distinctive IWs signatures. Indeed, a careful inspection of Figures 1b and 1d reveals periodic fluctuations in the SSHA of different scales, from ~ 50 km to ~ 5 km. These SSHA organized fluctuations are likely associated with IWs generated on the Amazon shelf by semi-diurnal tides, and then propagating from the shelf to open ocean.

Note, SSHA fields available in L3 datasets, and could be used without any filtering. However, after visualizing these data (see Figures 2a and 2d), it is still preferable to apply a low-pass filter to remove along-track variations with wavelengths larger than 200 km (as it was applied to L2 SSHA data), which are probably related to meso- and large-scale ocean variabilities. The SSHA data, after applying the low-pass filter, are illustrated in the Figures 2b and 2e. By Comparing the Figures 2 and 1, it can be concluded that there is no significant differences between L3 and L2 data. Their differences are illustrated in Figures 2c and 2f. Some small differences, can be referred to the filters applied to the L3 products to get SSHA. Explained in the description of SSHA in L3 products, the L3 SSHA product is height of the sea surface anomaly with all corrections (Geocentric ocean tide height, mean sea surface height, mean dynamic topography, satellite calibration) applied, which is different than SSHA, that we calculated using L2 SSH. Along transect (TS) profiles, and all further calculations, are applied to L2 data in the next Sections.

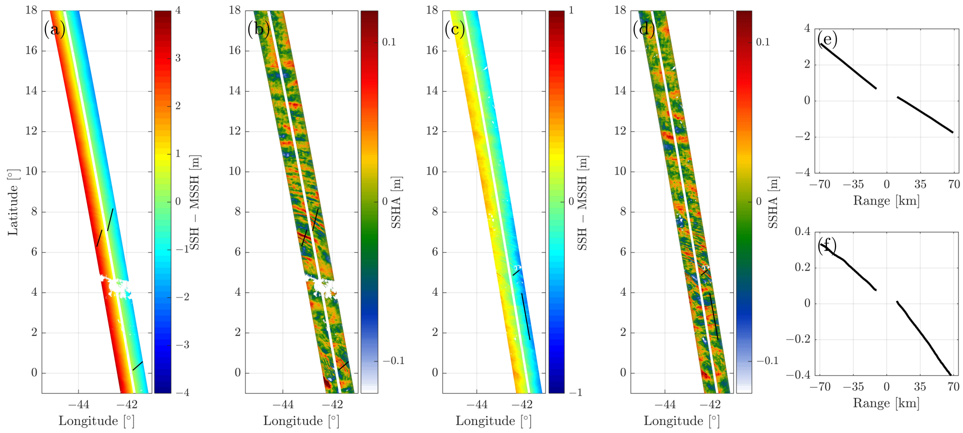

Figure 1: (a) and (c) Original SSHA off the Amazon shelf, and (b) and (d) SSHA, obtained by subtracting the mean SSH (plots e and f) from the original SSHA. Plots (a) and (b) are related to 09 May 2023, plots (c) and (d) – to 23 Jun 2023.

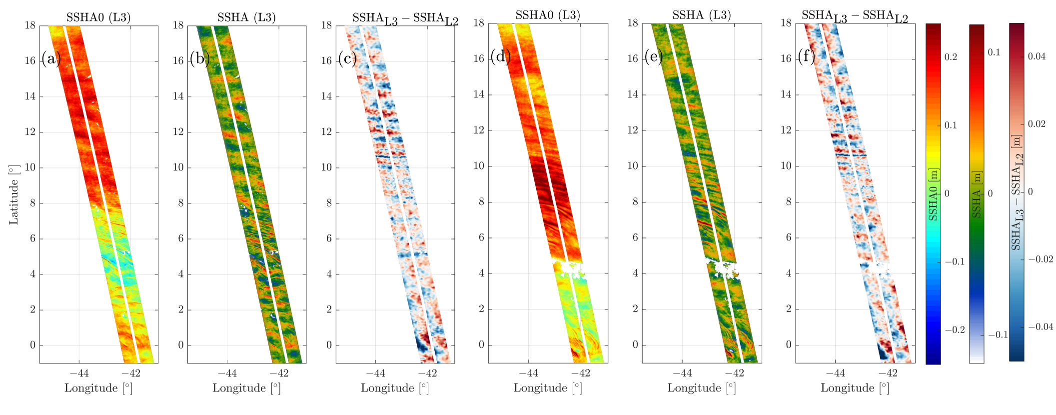

Figure 2: (a) and (d) L3 SSHA product; (b) and (e) SSHA after applying the low-pass filter to the L3 SSHA0; and (c) and (f) the differences between L2 (see Figures 1b and 1d) and L3 SSHA. Figures (a)–(c) shows data on 23 June 2023 and (d)–(f) on 09 May and off the Amazon shelf.

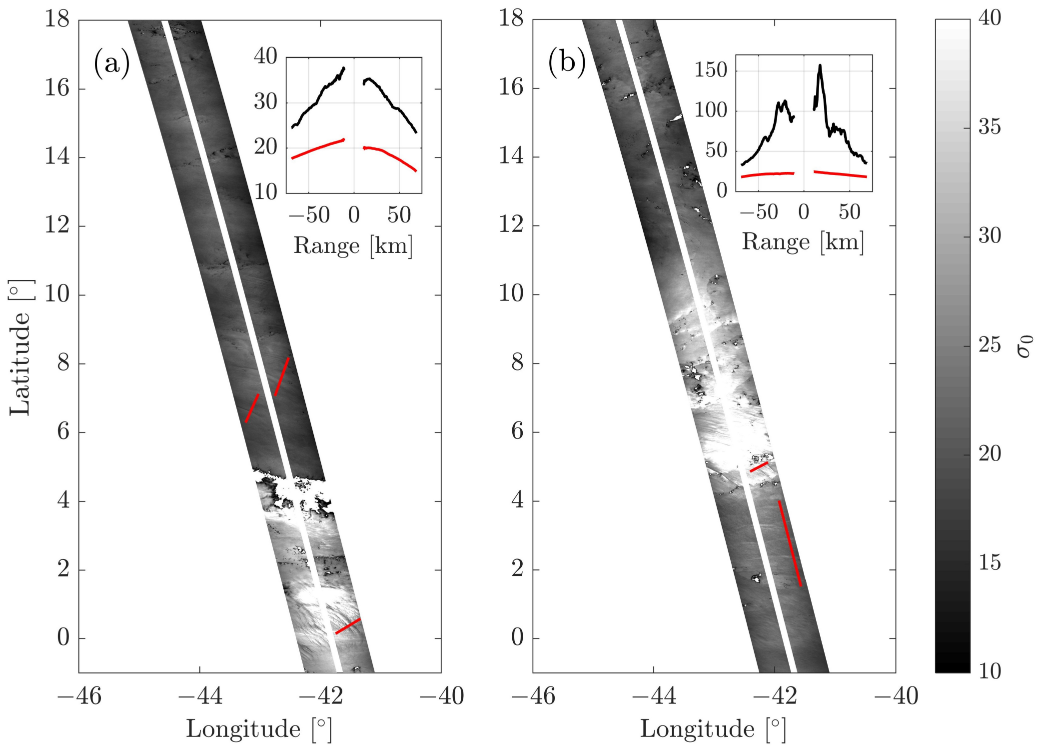

Figure 3: NRCS on (a) 09 May 2023, and (b) 23 Jun 2023 off the Amazon shelf in linear units. In the inserted graphs, the black and red line show the cross-track trend of σ_0 for areas of low wind (latitude rang of $-2° - +3°$ in (a) and $5.25° - 5.75°$ in (b)) and high wind (latitude rang of $6° - 16°$ in (a) and $-1°$ to $3°$ in (b)), respectively.

2.3 SWOT NRCS

The L2 unsmoothed SWOT data contain product for the sea surface NRCS in the range of incidence angles from 0.6° to 4° and −0.6° to −4° relatively to the nadir with spatial resolution, approximately, 250×250 m. Fields of the SWOT NRCS corresponding to Figures 1a and 1c, are shown in Figures 3a and 3b. Visually, Figures 3a and 3b exhibit well detectable IW signature in the NRCS image. Large scale variations of the NRCS are associated with the wind field variability. In particular, the brighter area indicates a low wind speed area, in agreement with European Centre for Medium-Range Weather Forecasts (ECMWF) reanalysis. Cross-track distributions of the NRCS shown in insert in Figure 3a exhibit the dependence of the NRCS on incidence angle. Clearly, the incidence angle dependence of NRCS is highly dependent on wind speed, ranging from weak at moderate wind speeds to quite strong at low wind speeds. Such a NRCS behavior is consistent with predictions of the classical radar scattering model for low incidence angles following quasi-specular reflections.

2.4 Data on Wind and Ocean Stratification

In this study, wind information are from the ECMWF atmospheric reanalysis, ERA5, with a temporal resolution of 1 hour and a spatial resolution of 0.25° × 0.25°.

To describe the state of the ocean interior, the monthly ocean salinity and temperature were obtained from the near real time multi observation global ocean ARMOR3D

L4 analysis and multi-year reprocessing. It consists of 3D temperature, salinity, geopotential heights, geostrophic Currents and mixed layer depth, available on a 1/4 degree regular grid and on 50 depth levels from the surface down to the depth of 5500 meters.

Salinity and temperature data are used to calculate vertical vertical distributions of the potential density, $\rho(z)$, which characterizes the ocean stratification via the Brunt–Väisälä frequency,

$$N^2 = \frac{g}{\rho_0}\frac{\partial \rho}{\partial z}, \tag{1}$$

where g is gravity acceleration and ρ_0 is the reference water density. To calculate $\rho(z)$, the Gibbs Sea Water (GSW) oceanographic toolbox of TEOS-10 was employed. Figure 4 displays the vertical profile of $\rho(z)$ and the Brunt–Väisälä frequency off the Amazon shelf during June 2023.

3 Reconstruction of IWs parameters

In this section, we consider the reconstruction of kinematic (wavelength and phase velocity) and dynamic (vertical displacement of ocean interior) properties of IWs, using observed SSHA estimates and available information on the ocean stratification state. SWOT SSHA, h, can be directly linked to the IW vertical velocity gradient below the surface which follows from continuity of the pressure through the ocean surface (Gill, 1982):

$$\hat{h}(K) = i\frac{C^2}{g}\frac{1}{\Omega}\hat{W}'_z|_{z=0} = \frac{C}{g}\hat{u}_s, \tag{2}$$

where hat denotes amplitude of the harmonic of any IW parameter which is function of IW wavenumber K, frequency, Ω, and phase velocity, and C (linked together through the dispersion relation), g is the acceleration due to gravity, $\hat{W}'_z$ is the vertical gradient of IW vertical velocity amplitude below the surface, i is the complex unit, and $\hat{u}_s$ is the horizontal velocity induced by IW on the ocean surface. Note that while the z-axis in this study is oriented downward, the SWOT SSHA in Equation 2 and subsequent equations is defined as positive when the ocean surface is displaced upward and negative when displaced downward.

From a knowledge of the ocean stratification, SWOT SSHA and detected IW wavelengths provide the necessary inputs to estimate the dispersion relation and the vertical velocity profile of IWs. Resulting displacements of the ocean upper layers can further be estimated. By integrating surface measurements with stratification data, it becomes possible to accurately describe the IWs impact on the deeper ocean layers.

3.1 Three-layer Approximation

3.1.1 Ocean Stratification

In the present study, a three-layer approximation is considered to describe the ocean stratification. In such an approximation, simple analytical solutions can be found for the IW dispersion relation and vertical modes, - similar to solutions derived in (Kudryavtsev, Monzikova, Combot, Chapron, Reul, & Quilfen, 2019; Kudryavtsev, Monzikova, Combot, Chapron, & Reul, 2019).

The three-layer approximation of ocean stratification adjusts the seasonal and the main pycnoclines with linear approximations of density over the depth, and the abyssal part with a constant density. The depth of the lower boundary of the main pycnocline, is defined as the depth of the layer containing 95 percents of the total observed density drop from the ocean surface to the bottom. The fit parameters, i.e. Brunt-Väisälä frequency, N, thickness of seasonal and main pycnoclines, are derived using a least squares method. Examples of this three-layer approximation on observed density and the Brunt–Väisälä

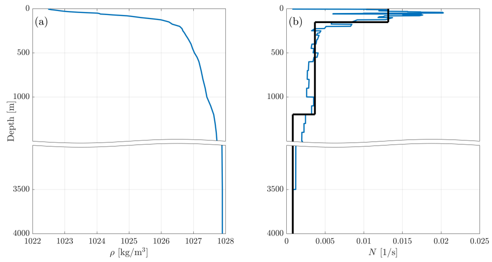

Figure 4: (a) Water density, and (b) Brunt–Väisälä frequency, N, off the Amazon shelf (Atlantic ocean) in June 2023. The black lines in the plots (b), show the three-layer approximation of Brunt-Väisälä frequency.

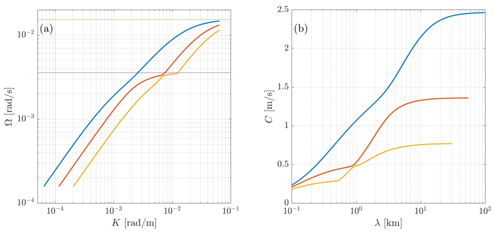

Figure 5: (a) Dispersion relation in form $\Omega = \Omega(K)$, and (b) in form of $C = \Omega/K$ against $\lambda = 2\pi/K$ defined by Equation A13 in Appendix A, and calculated for stratification shown in Figure 4. The curves marked by blue, flame and yellow colors, show the dispersion relation for the first three modes, respectively. The green and violet horizontal lines in (a), are the Brunt-Väisälä frequency for first and second layer (N_1 and N_2).

frequency, profiles are shown in Figures 4a and 4b, respectively. The three-layer approximation of Brunt-Väisälä frequency are marked by black lines in Figure 4b.

3.1.2 IW Dispersion Relation and Vertical Structure

Following this three-layer approximation, the Brunt–Väisälä frequencies, N, in each of the layers are constants (N_1, N_2, and $N_3 = 0$). The governing equation for internal waves (IW), Equation A1 in the Appendix A, has an analytical solution that provides the vertical velocity profiles $\hat{W}$ for IW harmonics (Equations A5–A7) and the dispersion relation (Equation A13), which links the IW frequency Ω to the wavenumber K.

The IW dispersion relations $\Omega = \Omega(K)$ (and in form $C = \Omega(K)/K$) for the first three modes of the given ocean stratification (shown in Figure 4 for June 2023 off the Amazon shelf), are displayed in Figure 5. The profiles of the vertical velocity for the first mode and different IW wavelengths are presented in Figure 6. These profiles reveal that the maximum vertical velocity amplitude occurs at different depths depending on the wavelength. Specifically, for wavelength, $\lambda = 1000$ m , the maximum vertical velocity, W, appears at the depth of 120 m, aligning with the upper boundary of the main pycnocline, shown in the Figure 4b. In contrast, for longer IWs, the maximum W is found at greater depths close to the lower boundary of the pycnocline.

3.2 SWOT SSHA interpretation

Within this framework, the pressure continuity condition at the ocean's surface, Equation 2, provides a relationship between the scale of IW vertical velocity, A, used for

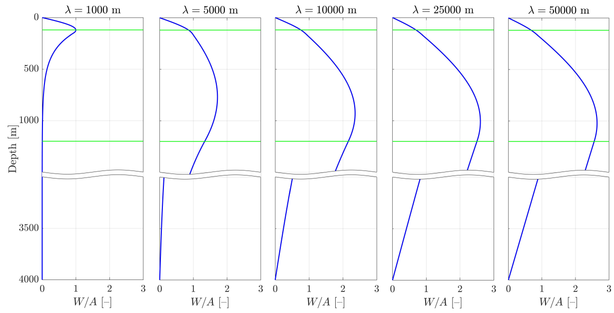

Figure 6: Vertical velocity profile, $W(K, z)$, for the IW first mode of different wavelengths, normalized by scale A, which is related to the SSHA by Equation A8. The green horizontal lines indicate the upper and lower boundary of the main pycnocline, shown in the Figure 4b

the scaling of vertical velocity profile described by Equations A5–A7, and the Fourier amplitude of SSHA, $\hat{h}$, measured by SWOT:

$$A(K) = -i\frac{g}{C}\frac{\Omega}{\sqrt{N_1^2 - \Omega^2}}\hat{h}(K), \tag{3}$$

Further, the vertical displacement of the pycnocline, $\eta(t, x, z)$, can be derived from the vertical velocity, $w(t, x, z)$, as: $w = \partial\eta/\partial t$. The scale of the pycnocline displacement, A_η, is related to the scale of vertical velocity as $A = -i\Omega A_\eta$, and hence be expressed through the measured amplitude of SSHA as

$$A_\eta(K) = \frac{g}{C\left(N_1^2 - \Omega^2\right)^{1/2}}\hat{h}(K) \tag{4}$$

For $N_1 \sim 10^{-2}$ 1/s and $C \sim 2$m/s, a SSHA with amplitude $\hat{h} = 0.1$m is equivalent to a pycnocline displacement of $A_\eta = 50$m. Using the Equation A5–A7 for vertical velocity profile, the expression describing the pycnocline undulation in physical space reads:

$$\eta(t, x, z) = i\int \Omega^{-1}\hat{W}(K, z)\exp i(Kx - \Omega t)d\Omega, \tag{5}$$

where only the real part has a physical meaning.

To illustrate this method to reconstruct the IW vertical structure using SWOT measurements, a fragment of the SWOT data shown in Figure 1d is selected. An enlarge image is shown in Figure 7a. The SSHA profile, $h(x)$, along the transect is shown in Figure 7b. A Fourier transform of the measured $h(x)$ is performed, $\hat{h}(K)$, which are shown in Figure 7c. Using Equation 4, the Fourier amplitude of the pycnocline displacement scale, A_η, is defined. Spatial variation of the pycnocline displacement, $\eta_0(x) = \int A_\eta \exp i(Kx)dK$, are shown in Figure 7d. For such a case, IW-induced pycnocline displacements are large, attaining -60 m in the trough and $+20$ m in the crest.

Ocean interior vertical displacements caused by the passage of IW trains calculated using Equation 5, are shown Figure 8a. The displacements of oceanic layers are maximum in the region of the IWs leading front (shown in Figure 7a and 7b), and are located at a depth of about 1200 m, corresponding to the lower boundary of the main pycnocline (see the Figure 4b). By comparing Figure 8a with Figure 7b and Figure 7d, it turns out that maxima of displacements caused by shorter IW harmonics, with wavelengths smaller than the leading edge, are located at smaller depths. The same vertical

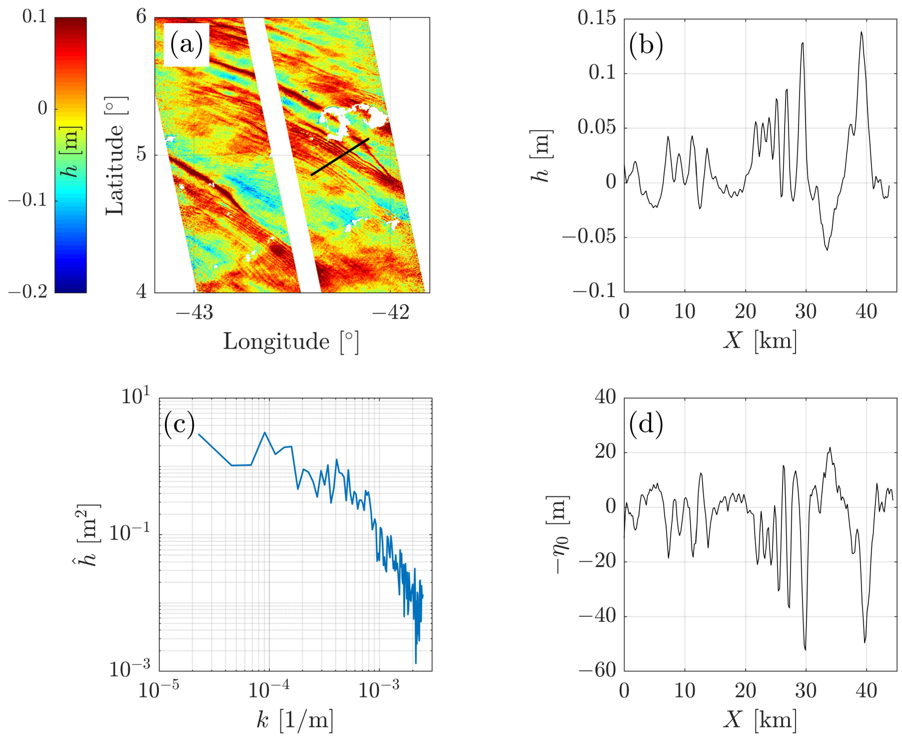

Figure 7: (a) Enlarge fragment of SSHA on 23 Jun 2023 and TS-4; (b) SSHA along the transect TS-4 marked by black line in (a); (c) square of amplitude of $\hat{h}$ as a function of wavenumber; and (d) the pycnocline displacement $\eta_0(x) = \int A_\eta \exp i(Kx)dK$ along the transect marked by black line in (a).

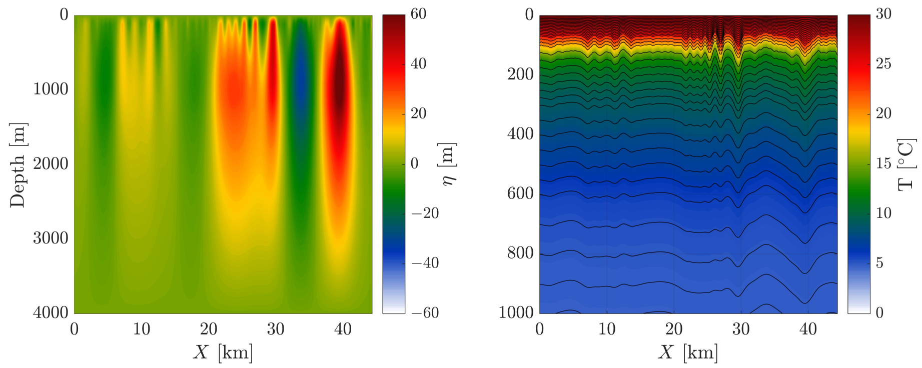

Figure 8: (a) Vertical structure of displacement, η, defined by Equation 5, and (b) IW-induced isotherms oscillations (contour lines).

displacement expressed in terms of the water temperature undulations are shown in Figure 8b. These calculations were performed assuming adiabatic variation of the water temperature:

$$T(z,x) = T_0(z - \eta(z,x)), \tag{6}$$

where $T_0(z)$ is the undisturbed temperature profile in the ocean. Results shown in Figure 8b confirm that the range of IW-induced isotherm displacements reaches ~ 100 m, largely related to the low-frequency components that compose the leading edge of the IW train. Isotherm displacements associated with the IW high-frequency components disappear at large depths, due to the rapid decay of the first mode with depth as it follows from Figure 8b.

4 Modulation of SWOT NRCS by IWs

4.1 Interpretation and Quantification

SWOT NRCS are dominated by quasi-specular reflections of the Ka-band radiowaves from the sea surface. In this case the NRCS of the sea surface, σ_0, can be described using the geometric optics approximation (Valenzuela, 1978):

$$\sigma_0 = (R^2 \sec^4\theta / s^2) \exp\left[-\tan^2\theta / s^2\right], \tag{7}$$

where R is the Fresnel coefficient, θ is incidence angle, s^2 is the mean square slope of the sea surface (MSS) in the range of surface waves wavenumber $K < nk_R$, where k_R is the wavenumber of radar wavelength ($k_R = 2\pi/0.008$ rad/m for SWOT) and n is a parameter which divides the surface on large-scale and small-scale surface. This division can be set as $n = 1/4$ (Voronovich & Zavorotny, 2001). Using Equation 7, the MSS is assumed isotropic (i.e. independent on direction relative to the wind direction) which is an acceptable approximation (Cox & Munk, 1954).

Accordingly, the IW σ_0 modulation is caused by the MSS modulation. Assuming that both the modulated amplitudes of the NRCS, $\delta\sigma_0$, and MSS, δs^2, are small relative to their mean values, $\overline{\sigma_0}$ and $\overline{s^2}$ correspondingly, the relationship between NRCS and MSS IW-induced modulations reads

$$\frac{\delta\sigma_0}{\overline{\sigma_0}} = \left(\frac{\tan^2\theta}{\overline{s^2}} - 1\right)\frac{\delta s^2}{\overline{s^2}}. \tag{8}$$

Consequently, SWOT NRCS signatures of IWs relate to the impact of IWs on the sea surface MSS.

To quantify these MSS modulations, a Modulation Transfer Function (MTF), $M_s(K)$, is used. This MTF will relate the MSS and the NRCS modulations scaled by their corresponding mean values (hereinafter termed as the contrasts: $K_{\sigma 0} = \delta\sigma_0/\overline{\sigma_0}$ and $K_s = \delta s^2/\overline{s^2}$) to a dimensionless IW parameter characterizing its intensity (non-linearity). Usually, such a IW parameter is $\hat{u}_s/C$, the ratio of the amplitude of the horizontal velocity induced by IW on the surface, $\hat{u_s}$, to its phase velocity, C. This parameter is equivalent to the divergence of the horizontal surface velocity induced by an IW on the ocean surface, $\partial u_s/\partial x$, scaled by the IW frequency, Ω. For harmonic oscillation, it is $\hat{D} = i\hat{u_s}/C$.

Using the continuity equation $iK\hat{u_s} = -\hat{W}'_z|_{z=0}$ and the pressure continuity across the surface, Equation 2, the scaled divergence can be rewritten in terms of the amplitude of measured SSHA as:

$$\hat{D}(K) = -i\frac{g}{C^2}\hat{h}(K). \tag{9}$$

The following definition of MTF for the MSS modulations becomes:

$$\hat{K_s}(K) = M_s(K)\hat{D}(K) = -iM_s(K)\frac{g}{C^2}\hat{h}(K). \tag{10}$$

Correspondingly, following Equation 8, the SWOT NRCS modulations are related to the amplitude of SWOT SSHA anomalies as:

$$\hat{K}_{\sigma 0}(K) = -iM_s(K)\left(\frac{\tan^2\theta}{\overline{s^2}} - 1\right)\frac{g}{C^2}\hat{h}(K). \tag{11}$$

Finally, the contrasts of NRCS and MSS variations in the physical space, $K_{\sigma 0} = \delta\sigma_0/\overline{\sigma_0}$ and $K_s = \delta s^2/\overline{s^2}$, are obtained as

$$K_q(x) = \int \hat{K}_q(K)\exp\left[i(Kx - \Omega t)\right]dK, \tag{12}$$

where subscript q denotes s and/or σ_0 with amplitudes $\hat{K}_q(K)$ given by Equation 10 and/or Equation 11. To analyze the observed NRCS variations caused by IWs, it will also be helpful to use the divergence of IW-induced surface currents derived from h in physical space, which from Equation 9 reads

$$D(x) = -i\int \frac{g}{C^2}\hat{h}(K)\exp\left[i(Kx - \Omega t)\right]dK, \tag{13}$$

where only the real part has a physical meaning.

Schematic representation of SWOT imaging of IWs according to Equations 8–11 is shown in Figure 9. Wind waves propagating through oscillating IW-induced surface currents are modulated, causing periodic changes in MSS that correlate with surface current divergence. Spatial variations of the MSS lead to inverse oscillation in the surface NRCS which are displayed in the SWOT data as dark/bright patterns.

4.2 Observations

Correlation between SWOT SSHA and NRCS variations can be visually identified on the enlarged fragments presented in the Figure 10. The SWOT L2 products also contain wind information (speed and direction) from ECMWF, presented in the Figures 10c and 10f. For transects TS-1 and TS-4 wind speed is ≤ 7 m/s, while for other transects (TS-2 – TS-3 and TS-5) wind speed is ~ 10 m/s, with southwest direction on TS-2–TS-3 and northeasters one on TS-3 transect. By comparing the wind speed and NRCS from the Figure 10, it is visible that the NRCS have larger values for lower wind condition. The values for averaged wind speed, $\overline{U}_{10}$, wind direction, $\overline{\varphi}_w$, and propagation direction of IW, $\overline{\varphi}_{\text{IW}}$ on the transects are listed in the Table 1

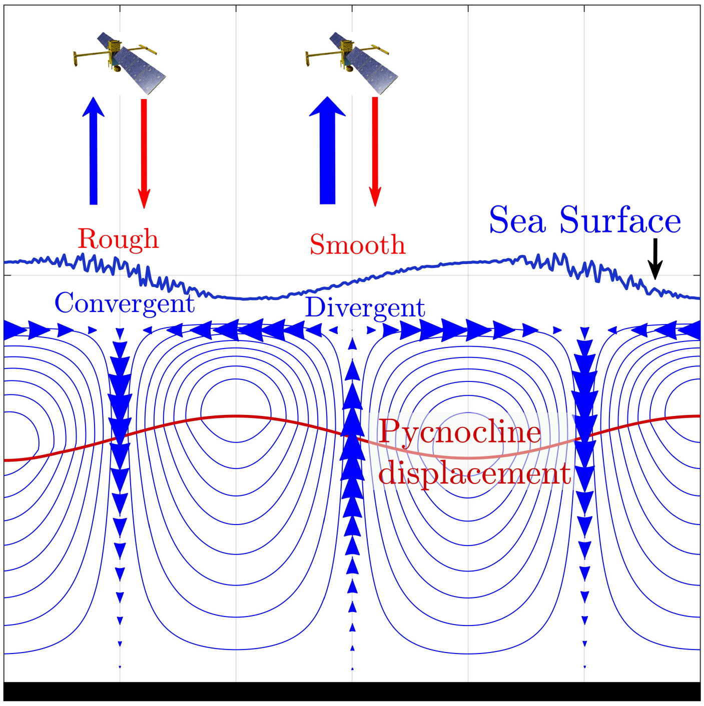

Figure 9: Schematic representation of SWOT imaging of IWs. Vertical red and blue arrows show transmitted and received signal after its reflection from the sea surface. The width of the blue arrows is proportional to the power of the reflected signal, which in turn is inversely proportional to the mean square slope of the sea surface (MSS). Modulations of the MSS are caused by interaction of wind waves with surface currents induced by IW. Blue contours and arrows indicate velocity field in IW. In this case enhancement/suppression of MSS occurs in the zones of surface currents convergence/divergence which are respectively displayed in the SWOT data as dark/bright patterns.

Table 1: IWs and wind parameters for each of the transects

	std($K_{\sigma 0}$) [–]	std(D) [–]	$\overline{C}$ [m/s]	$\overline{U}_{10}$ [m/s]	$\overline{\varphi}_w$ [°]	$\overline{\varphi}_{IW}$ [°]
TS-1	0.14	0.05	2	3	164	44
TS-2	0.027	0.054	1.84	10	217	77
TS-3	0.021	0.08	2.05	9	226	76
TS-4	0.063	0.07	1.73	7	132	42
TS-5	0.011	0.031	1.96	10	140	100

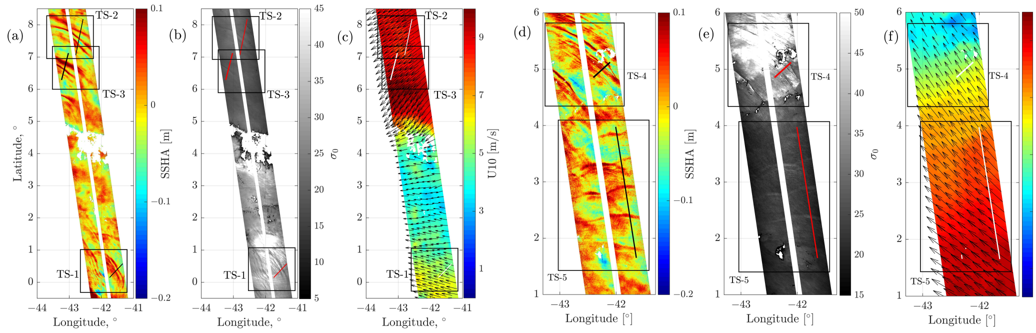

Figure 10: Enlarged fragments of: (a) and (d) SSHA, (b) and (e) σ_0 in linear units, (c) and (f) ECMWF wind fields on 09 May (a–c) and 23 Jun (d–f) 2023. The transects analyzed below are designated TS-1 – TS-5.

4.2.1 Qualitative analysis

Transects of the enlarged fragments in Figure 10 denoted as TS-1 – TS-5 are shown in the upper row of Figures 11–15 respectively. The NRCS contrasts ($K_{\sigma 0}$) and SSHA (h) along each of the transects represent the values which are averaged over a 2 km wide strip. In addition, the IW surface current divergence scaled by frequency, $D(x)$, derived from SSHA according to Equation 13 is also shown in the lower row of Figures 11–15. This quantity is considered as the governing parameter driving manifestation of IW on the sea surface roughness, and thus the MSS and NRCS variations expressed via the MTF in Equation 11 and Equation 10. For quasi-monochromatic oscillations, the quantity D is equivalent to the ratio of the amplitude of IW-induced surface current variations to the IW phase velocity.

In Figure 11, the TS-1 crosses the IWs train under low wind speed conditions. IW wavelength is about 10 km, estimated from the periodic variations of $K_{\sigma 0}$, h and D shown Figure 11d and Figure 11e. Oscillations with shorter length ($<$ 5 km) are visible as well. All in all, $K_{\sigma 0}$ variations are visually correlated with h. A spatial shift is also identified, the maximum values of $K_{\sigma 0}$ being located somewhere between the crests and troughs of h. The correlation between $K_{\sigma 0}$ and surface current divergence, D, is visually better pronounced and spatially more synchronized. NRCS enhancements/diminution are taking place in surface current convergence/divergence areas, as schematically explained Figure 9. The standard deviation of $K_{\sigma 0}$ and D are 0.14 and 0.05, respectively. The ratio gives an estimate of the MTF: $M = \mathrm{std}(K_{\sigma 0})/\mathrm{std}(D)$, which is about 3 for this case.

Figure 12a shows an IW train under higher wind speed conditions, also clearly appearing in the field of the NRCS, Figure 12b. Wavelengths of this train are $\sim 20 - \sim 33$ km (see Figure 12d). Unlike the previous case TS-1, crests/troughs of SSHA h coincide with darker/brighter NRCS features, Figure 12d. Consequently $K_{\sigma 0}$ is shifted on $\pi/2$ relative to the convergence/divergence zones, Figure 12e. A possible reason is the differing wind conditions. The standard deviation of $K_{\sigma 0}$ and D for this case are 0.03 and 0.09, respectively. It gives a much lower (compared to TS-1) estimate of the MTF, about 1/3.

Figure 13a display the case of an internal solitary wave,Figure 13a, and its related NRCS manifestation, Figure 13b, also under high wind speed conditions, Figure 13c. The crest of this wave in SSHA is clearly distinctive on Figure 13d. NRCS contrasts and the solitary IW are clearly linked, Figure 13d). NRCS variations are rather associated to the surface currents divergence induced by this solitary IW (Figure 13e). Ratio of peak-over-

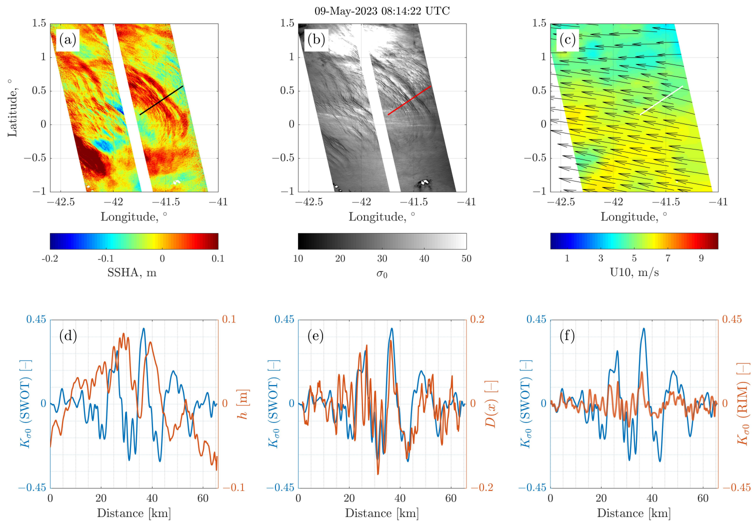

Figure 11: Upper row, maps of: (a) SSHA, (b) NRCS, and (c) wind field. Lower row, transects of: (d) $K_{\sigma 0} = \delta\sigma_0/\overline{\sigma_0}$ (blue) and SSHA (red), (e) $K_{\sigma 0}$ (blue) and surface current divergences scaled by frequency, D (red), (f) SWOT $K_{\sigma 0}$ (blue) and $K_{\sigma 0}$ from RIM simulations (red). In Figures (d)–(f) the left axis is $K_{\sigma 0}$ from SWOT observations.

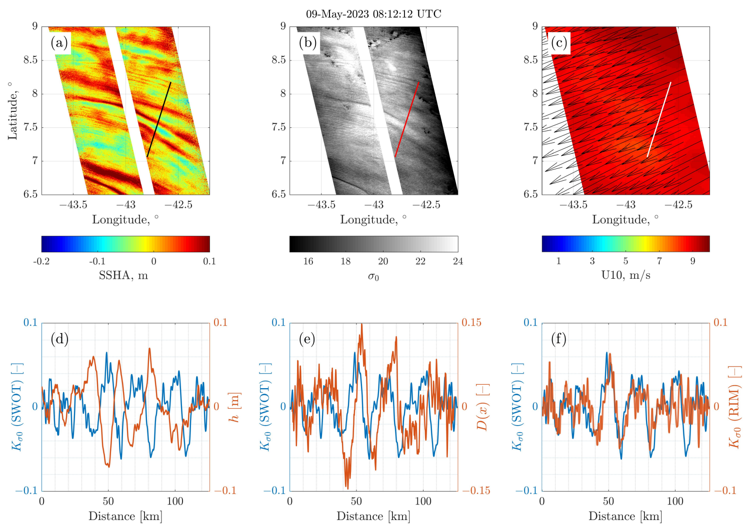

Figure 12: The same as Figure 11, but for TS-2.

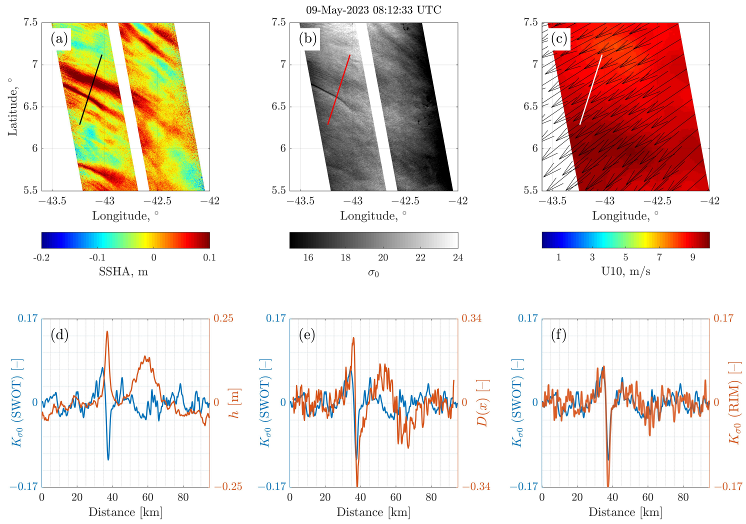

Figure 13: The same as Figure 11, but for TS-3.

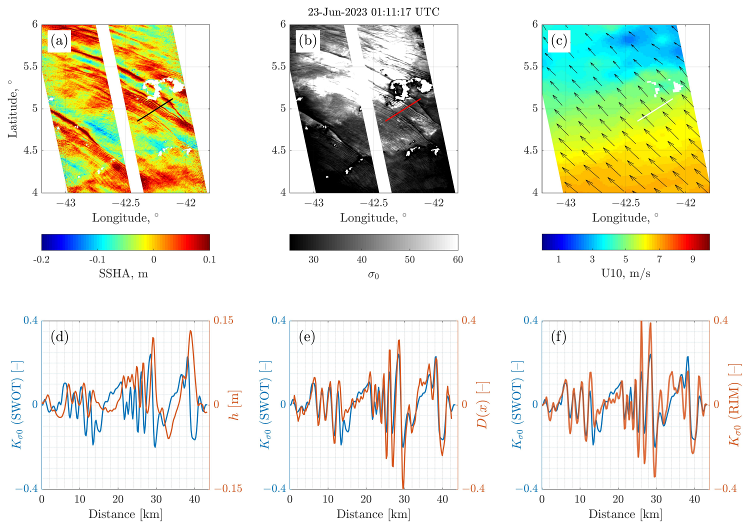

Figure 14: The same as Figure 11, but for TS-4.

trough value for $K_{\sigma0}$ (which is about 0.15) to peak-over-trough value for D (which is about 0.7), evaluated for solitary IW in Figure 13e, gives an MTF of about 0.2.

Figures 14 and 15 illustrate IWs from SWOT acquisitions on 23-Jun-2023. The leading solitary IW and the two IWs trains following it are clearly distinguishable, either in SSHA, Figure 14a, and in NRCS, Figure 14b. IWs signatures along the transect of SSHA, Figure 14d, are especially well detected in the divergence area of the IWs surface current, Figure 14e. In this case IW-induced contrasts of the NRCS, $K_{\sigma0}$, are very well correlated with the current divergence, see (Figure 14e). The large values of NRCS contrasts is probably associated with weak wind conditions. The wind speed is about $U10 = 5$–7 m/s, Figure 14c and provides favorable conditions for IWs to imprint large sea surface roughness variations. In this case, the standard deviation of $K_{\sigma0}$ and D are 0.09 and 0.13, i.e. the MTF is rather large, about 0.7.

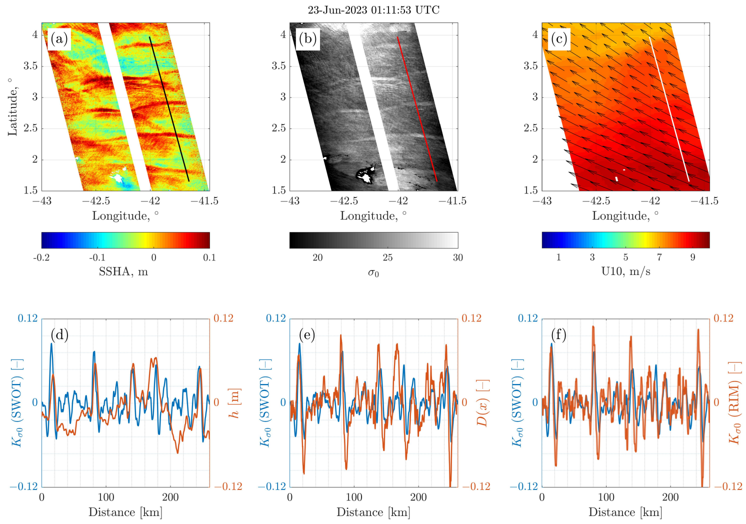

Figure 15: The same as Figure 11, but for TS-5.

Figure 15a and Figure 15b present SWOT observations for a case of long IWs (with wavelength of ~ 50 km). The only thing that distinguishes this case from the previous ones and deserves special attention, is the direction of the wind. For this case, the wind aligns with the IW propagation direction, see Figure 15c. Visually, good correlation are again obtained between the NRCS variations, Figure 15b and SSHA, Figure 15a, for these large-scale IWs. Profiles of the SSHA and NRCS variations along the transect, Figure 15d and Figure 15e, show that the NRCS maxima are located in the zones of surface currents divergence of large-scale IWs. The ratio of the peak-to-trough difference for $K_{\sigma0}$ (about 0.1) to the peak-to-trough difference for D (about 0.2) suggests a MTF estimate of about 0.5.

4.2.2 Spectral analysis

A spectral analysis is performed for the data acquired along transects TS-1 to TS-5, using the Welsh method (Welch, 1967). Co-spectra of SSHA, $h(x)$ and NRCS contrasts, $K_{\sigma0}(x)$, termed $S_h(K)$ and $S_\sigma(K)$, correspondingly, and cross-spectra, $S_{h\sigma}(K)$, are derived and reported in Figure 16. To implement Welch's method, the FFT length is set to 1/4 of the realization length, applying 50% overlap, and a Hamming window. Number of samples for each section in Hamming window is equal to the FFT length. The sampling wave number is given by $K_s = 1/\Delta x$ with $\Delta x = 200$ m.

Using Equation 9 and dispersion relation described in Appendix A, spectra of SSHA are further converted to co-spectra of IW-induced surface current convergence:

$$S_D(K) = \left(\frac{g}{c^2}\right)^2 S_h(K), \tag{14}$$

and cross spectra between NRCS variations and the IW divergence:

$$S_{D\sigma}(K) = -i\frac{g}{C^2} S_{h\sigma}(K), \tag{15}$$

Spectrum of coherence $\gamma(K)$

$$\gamma^2 = \frac{|S_{D\sigma}|^2}{S_D S_\sigma} = \frac{|S_{h\sigma}|^2}{S_h S_\sigma}, \tag{16}$$

is a quantitative measure of relationship between IW and NRCS variations. Combination of cross-spectra, Equation 15 and spectrum divergence, Equation 14 provide esti-

Table 2: The result of cross-spectral analysis for $K_{\sigma 0}$ and $D(x)$.

	λ [km]	$\gamma^2_{\max}$	ψ [°]	MTF
TS-1	~ 10	~ 0.91	~ 24	$2 \leq M \leq 3.5$
	~ 3	0.81	~ 63	0.91
TS-2	~ 18	~ 0.72	~ 78	~ 0.45
	~ 11	0.75	~ 90	0.7
TS-3	$5 \leq \lambda \leq 10$	~ 0.77	~ 60	~ 0.3
TS-4	$2 \leq \lambda \leq 10$	0.97	$-10 \leq \psi \leq 30$	$0.6 \leq M \leq 0.9$
TS-5	$10 \leq \lambda \leq 44$	0.8	$-82 \leq \psi \leq -33$	$0.23 \leq M \leq 0.9$

mates of the spectral MTF for the NRCS modulations:

$$M_{\sigma 0}(K) = \frac{S_{D\sigma}}{S_D} = -i\frac{C^2}{g}\frac{S_{h\sigma}}{S_h}. \tag{17}$$

MTF magnitude, $|M_{\sigma 0}|$, describes how strong is the response of the surface NRCS to IW, while the MTF phase, $\tan(\psi) = \mathrm{Im}(M_{\sigma 0})/\mathrm{Re}(M_{\sigma 0})$, defines the phase shift between NRCS and surface current divergence oscillations.

To obtain statistically significant MTF estimates, a confidence level for the coherence spectrum is evaluated as (Thomson & Emery, 2014):

$$\gamma^2_{1-\alpha} = 1 - \alpha^{[1/(D_f - 1)]}, \tag{18}$$

where α is linked to the percentage of confidence, and equal e.g. to $\alpha = 0.10$, 0.05, 0.01 for confidence intervals of 90, 95, 99% . Parameter D_f in Equation 18 is the number of independent cross-spectral realizations. Spectral estimates were obtained using FFT over 1/4 of the realization length, with 50% overlap. The degree of freedom is $D_f = 4$, and hence 95% confidence level for coherence is $\gamma^2_{95\%} = 0.63$. Only MTF values (estimated by Equation 17), falling into the wavenumber range where $\gamma^2 > \gamma^2_{95\%}$, are then retained.

Spectral analysis is performed for transects depicted in Figures 11–15, and resulting spectra for S_D and S_σ shown in Figure 16. For TS-1, maximum values for both spectra occur at a wavelength of approximately 12.5 km. However, the highest correlation (exceeding confidential level $\gamma^2_{95\%} = 0.63$) is found at a wavelength of 10 km, with a phase delay of 21°. For TS-2, maximum spectral values are around 25 km, while the maximum correlation occurs at 33 km with a phase delay of about 90°. For TS-3, TS-4, and TS-5, maximum correlations are observed at wavelengths of 9, 2.5, and 50 km, respectively. Corresponding phase delays are 50°, 20°, and −30°. The Table 2 lists the values of wavelength of dominant IW, phase delay, MTF amplitude, corresponding to the maximum values of γ^2 which exceed confidential level for all considered cases.

Figure 17 summarizes the derived MTF magnitudes depending on the IW wavenumber, Figure 17a, and wind speed, 17b. MTF magnitudes exhibit some growing trend with increasing wavenumber, until about $K < 10^{-4}$ 1/m, reaching a constant value for larger K. MTF amplitudes more clearly decrease with increasing wind speed, Figure 17b. Such wind trend is anticipated and was reported in earlier studies (e.g. Equation 3 in (Kudryavtsev

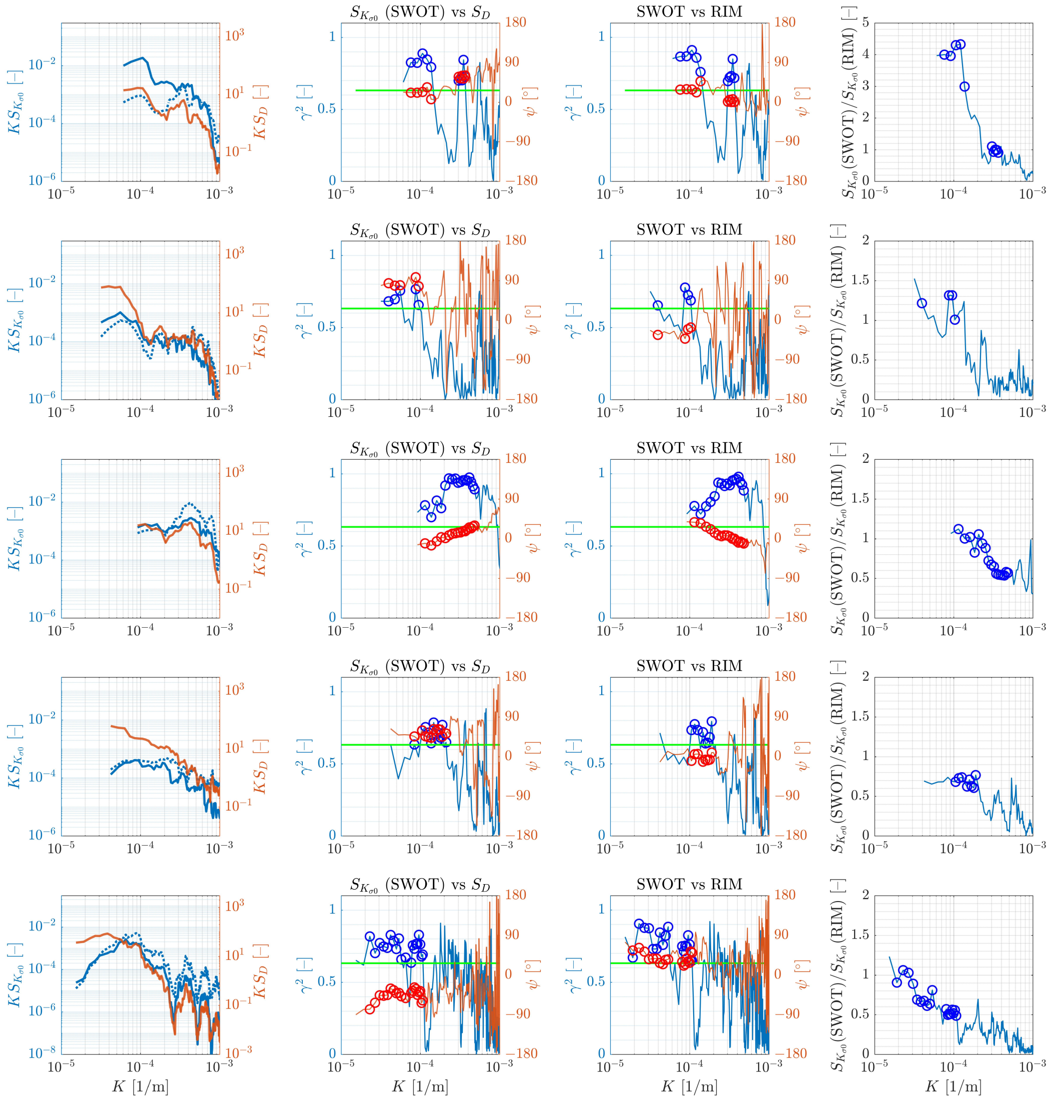

Figure 16: Columns from left to right: 1) Spectra of SWOT $S_{\sigma 0}(K)$ (solid blue), RIM-simulated $S_{\sigma 0}(K)$ (dotted blue) and $S_D(K)$ (flame); 2) Spectra of coherence, γ^2 (blue), and phase shift, ψ, (flame) between variations of the NRCS ($K_{\sigma 0}$) and the surface currents divergence (D); 3) Spectra of coherence, γ^2 (blue), and phase shift, ψ, (flame) between $K_{\sigma 0}$ observed by SWOT and $K_{\sigma 0}$ simulated using RIM; 4) Ratio of SWOT to RIM spectral amplitudes of $K_{\sigma 0}$ defined as $\gamma(S_{\sigma 0}^{SWOT}/S_{\sigma 0}^{RIM})^{1/2}$ where γ is SWOT-RIM coherence. Green lines in the second and third columns indicate confidential level for coherence $\gamma^2_{95\%} = 0.63$. Blue and red circles indicate values of co-spectral characteristics for which the coherence exceeds the confidence level.

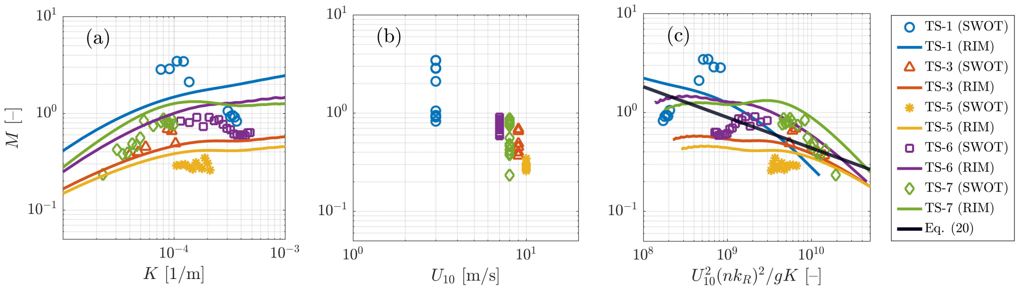

Figure 17: Magnitudes of NRSC-IWs MTF, $|M\sigma 0|$, Equation 17, as a function of wavenumber (a), wind speed (b) and dimensionless parameter $k_R^2 U_{10}^2/gK$ (c). Symbols,-circles, triangles, stars, squares, and diamond, correspond to spectral estimates of TS1–TS7 in Figure 16 respectively whose γ^2 exceeds $\gamma^2_{95\%}$. Lines are RIM simulations of $|M\sigma 0|$. Color coding for the symbols and curves is specified in the legend.

et al., 2012)). As an attempt, MTF estimates may be compared to a dimensionless variables. As a dimensionless variable, we consider the ratio between the IW wavelength, $1/K$ and the wind waves relaxation scale, $l \propto 1/(\beta k)$, where $\beta \propto (U_{10}^2/c^2)$ is the wind waves growth rate, k and c are wavenumber and phase velocity of a surface wave. Taking the SWOT radar wavenumber k_R as a typical scale for the upper bound of the wavenumber interval of short wind waves, whose MSS parameters control the sea surface NRCS (see Equation 7), the dimensionless parameter becomes $\beta k/K \propto k_R^2 U_{10}^2/(gK)$. MFT magnitudes as a function of this parameter are presented Figure 17c. The use of this dimensionless variable does not lead to significant improvements. This suggests that an additional information is likely needed. To first order, the angle between the wind direction and IW propagation can be suggested to play an important role. Nevertheless, a first guess to fit MTF data is

$$|M_{\sigma 0}| = 10^{2.74\pm 1.25}\left(\frac{k_R^2 U_{10}^2}{gK}\right)^{-0.31\pm 0.13}, \tag{19}$$

which provides the order of expected NRCS variations caused by IW (black line in Figure 17c).

4.2.3 Radar Imaging Model

To further investigate and quantify SWOT NRCS contrasts, the radar imaging model (RIM) suggested by Kudryavtsev et al. (2005) and Johannessen et al. (2005) is considered. Within the RIM framework, MSS contrasts induced by IW read

$$\hat{K}_s(K) = \frac{\int\int_{k<k_d} T(\mathbf{k}, K) B(\mathbf{k}) d\phi d\ln k}{\int\int_{k<k_d} B(\mathbf{k}) d\phi d\ln k} \tag{20}$$

where $T(\mathbf{k}, K)$ is a spectral transfer function, $B(\mathbf{k})$ is the surface wave saturation spectrum, $\mathbf{k}$ is the surface wave wavenumber vector, k and ϕ its module and direction. The spectral transfer function $T(\mathbf{k}, K)$ is related to the spectral MTF used in the present work as follows: $T(\mathbf{k}, K) = M(\mathbf{k}, K)\hat{D}(K)$. In RIM, the spectral transfer function $T(\mathbf{k}, K)$ is given by Equation 48 in (Kudryavtsev et al., 2005). When applied to MSS modulations, this equation can be simplified and rewritten in terms of spectral MTF as:

$$M(\mathbf{k}, K) = \frac{\tau\Omega/\omega}{1+ir}\left[m_k \cos^2\phi + \frac{c_{wb}}{B(\mathbf{k})}\int\int_{k'<\frac{k}{10}} \frac{m_k \cos^2\phi}{1+ir} B d\phi d\ln k'\right] \tag{21}$$

where r is a relaxation parameter defined by $r = (\tau\Omega/\omega)(\cos\phi c_g/C - 1)$, c_g is the wave group velocity, τ is dimensionless relaxation time, see Equation (42) in (Kudryavtsev et al., 2005), $m_k(\mathbf{k}) = d\ln(N(\mathbf{k}))/d\ln(k)$ is the spectral wavenumber exponent, with $N(\mathbf{k})$ the wave action spectrum, and $c_{wb} = 1.44$ is a model constant. The first term on the right side of Equation 21 describes spectral modulations caused by the direct interaction of waves with varying surface currents. The second term describes the mechanism of cascade modulations of short waves, associated with sea surface mechanical disturbances caused by modulations of breaking of longer wind waves. The spectral MTF is explicitly dependent on the angle between the wind and IW directions through the parameter r in the denominator of Equation 21. Referring to this equation, modulations caused by IWs are maximum in the spectral range for which a group resonance between surface and internal waves occurs, i.e. the condition $\cos\phi c_g/C - 1 = 0$ is satisfied.

To calculate the Fourier component of MSS contrasts using Equation 21 with $T(\mathbf{k}, K) = M(\mathbf{k}, K)\hat{D}(K)$, it is necessary to specify the input parameters: surface current, which appear in Equation 9 as Fourier harmonic of the surface current divergence ($\hat{D}$); IW wavenumber (frequency and phase speed follow from dispersion relation); wind speed and wind direction relative to the IW direction; and inverse wave age (U_{10}/c) of the spectral peak of wind waves. In this work, the latter is taken equal to 1. Other parameters required to perform calculations, i.e. the background spectrum $B(\mathbf{k})$, wavenumber exponent $m_k(\mathbf{k})$ and relaxation time τ, are coming from the solution of the background RIM model, detailed in (Kudryavtsev et al., 2005) and not repeated here.

To compare the RIM results with the observed $K_{\sigma 0}$ (which is related to K_s through Equation 21), SWOT SSHA estimates are converted to the surface current velocity divergence using Equation 2. Other required input parameters are specified as: incidence angle is set to 2° (the middle of each swath); radar wavelength to 8 mm (Ka band); wind speed as the along-transect averaged wind; phase velocity (and frequency) of IWs calculated using the dispersion relation for each Fourier harmonic in wavenumber space, the superposition of which describing variations in IW-related variables in physical space. Input parameters used in RIM simulations are listed in the Table 1.

RIM results are shown on Figures 11f, 12f, 13f, 14f, and 15f. While the general shape of RIM-simulated NRCS contrasts is similar to observed ones, suggesting they are well phase-synchronized, apparent discrepancies are found for the amplitude of $K_{\sigma 0}$. For TS-1, Figure 11f, the RIM-simulated amplitude $K_{\sigma 0}$ matches observations over regions where SWOT shows low $K_{\sigma 0}$ modulations. But, over areas where SWOT indicates high $K_{\sigma 0}$ amplitudes, RIM simulations underestimate the observed amplitudes. Discrepancies are also evident in TS-3, single explosives in Figure 13f, TS-4 Figure 14f, and TS-5, long explosives detected in Figure 15f, where RIM model seemingly overestimates SWOT observations for the strongest oscillations caused by IW. These discrepancies may be explained either by uncertainty in the low wind speed/direction estimates and/or by the calibration of the SWOT products, but also RIM imperfections.

Relationships between the RIM simulations and the SWOT observations of IW-induced NRCS contrasts, from their cross-spectral analysis, are presented in the third column of Figure 16. A high level of coherence (exceeding the confidence level $\gamma^2_{95\%} = 0.63$) between RIM and SWOT $K_{\sigma 0}$ is obtained in the same range of IW wavenumbers for which a high correlation between SWOT $K_{\sigma 0}(x)$ and $D(x)$ occurs (compare γ^2 in the second and third columns of Figure 16). The phase shift between the RIM and SWOT $K_{\sigma 0}(x)$ is noticeable, but it is within the 95% confidence interval of the phase estimate. The last column in Figure 16 shows the ratio of observed spectral amplitudes of $K_{\sigma 0}$ to RIM ones, defined as $\gamma(S_\sigma^{SWOT}/S_\sigma^{RIM})^{1/2}$ for $\gamma > \gamma_{95\%}$. These values quantify how acceptable is RIM to simulate SWOT observations. Besides the TS-1 case, RIM is satisfying.

RIM estimates of the spectral MTF are shown Figure 17a as function of IW wavenumber, and Figure 17c, as function of dimensionless parameter $k_R^2 U_{10}^2/(gK)$. From this Figure, RIM simulations lead to varying curves in relative agreement with the data spread. Representing RIM simulations in dimensionless variables, Figure 17c, does not reduce this observed spread. It suggests that IWs signatures in SWOT NRCS are a multifactor process that cannot be described using a simple combination of input parameters, as done in Figure 17. The use of simplified physically based radar imaging models, such as RIM, may thus be preferable to the analysis and interpretation of SWOT observations rather than the use of ad hoc empirical models.

4.2.4 RIM predictions

SWOT observations reported here, although limited, indicate that the magnitudes of IW-induced NRCS modulations can greatly vary depending on wave parameters and environmental conditions. RIM is then derived for different wind speeds, from 2 m/s to 20 m/s, wind direction relative to IW propagation direction, from 0° to 180°, and IW wavenumber. For these calculations, the IW dispersion relation is specified in the form shown Figure 4.

Results are shown Figure 18, in terms of the MTF, Equation 21, for the sea surface MSS in the wavenumber range $k < 1/4k_R$. A main feature is an apparent strong dependency on azimuth, with maximum values when IWs propagate in the wind direction. This behavior is related to the resonance between surface and internal waves in the spectral interval of wind waves for which the wave group velocities can coincide with the IW phase velocity ($c_g = C$ in denominator of Equation 21). Consequently, wave-spectrum modulations in this interval are amplified, leading to enhanced MSS modulations. The resonance efficiency is also dependent on the wind speed, which determines the relaxation time $\tau \propto c^2/U_{10}^2$. As the wind increases, the resonance is suppressed, as well as modulations in other spectral intervals which are proportional to τ, Equation 21. This general feature of MSS modulations is well expressed in Figure 18. In addition, the relaxation time multiplied by the frequency of IW, leads to the fact that MSS modulations strongly depend on the IW wavelength, also clearly obtained in Figure 18. At small values of τ, the wave spectrum increases in regions of the surface currents convergence, leading to a coincident increase in the MSS. Such MSS features, inverted for the NRCS modulations, have already been noted in the analysis of SWOT measurements.

5 Conclusion

This paper provides new insights about internal waves (IWs) off the Amazon shelf using high-resolution data from the Surface Water and Ocean Topography (SWOT) mission, showcasing the KaRIn instrument ability to capture and quantify sub-mesoscale oceanic processes. Thanks to these newly available 2D altimeter fields, IW patterns can be clearly identified, extending beyond the Amazon shelf. Distinct periodic signatures are found, characterized by wavelengths ranging from 3 to 50 km and sea surface height anomalies (SSHA) ranging from several to about 20 centimeters.

A three-layer approximation to describe the ocean stratification is employed to reconstruct IW induced vertical motions from SWOT SSHA estimates. Within this framework, analytical expressions for the IW dispersion and orbital velocities are obtained. Using the pressure continuity at the sea surface, observed SSHA are also converted to estimate thermocline displacements caused by these IWs. As found, thermocline oscillations reach 80 m amplitudes. SWOT observations can thus uniquely inform about the ocean interior state, to more precisely evaluate the IW energy and its distribution over depth.

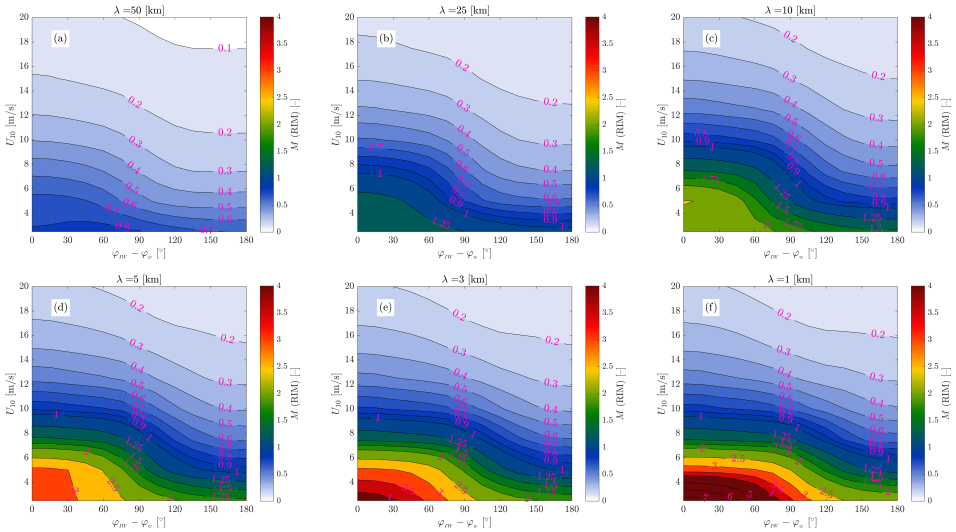

Figure 18: Modulation transfer function (MTF) for the sea surface MSS predicted by RIM, Equation 21 with $T(\mathbf{k}, K) = M(\mathbf{k}, K)\hat{D}(K)$, for IW with wavelengths of 50 km (a), 25 km (b), 10 km (c), 5 km (d), 3 km (e), and 1 km (f), in the wind speeds range from 2m/s to 20 m/s, and different wind directions relative to IW propagation, $\varphi_{\mathrm{IW}} - \varphi_w$, varying from 0 to 180 degrees.

SWOT SSHA estimates are further enriched by coincident ocean near-nadir normalized radar cross section (NRCS) measurements. For IWs, this provides a unique opportunity to study the mechanisms leading to measurable surface roughness modulations. SWOT SSHAs, converted to surface current velocity using fundamental dynamic laws, indeed provide necessary surface parameters to study wind wave and associated mean square slope of the sea surface (MSS) hydrodynamic modulations, and corresponding SWOT NRCS ones.

SWOT data are then analyzed in terms of a modulation transfer function (MTF), relating the SWOT NRCS contrasts to the divergence of the IW surface currents, normalized by the IW frequency derived from SWOT SSHAs. Obtained MTFs quantify the relationship between the NRCS contrasts, the amplitude and wavenumber of IWs, but also the local wind speed. Results clearly emphasize the significant role of wind speed and its direction (relative to IW propagation) to interpret NRCS modulations, with lower wind speeds enhancing the NRCS contrasts, facilitating the detection of IW features.

The Radar imaging model (RIM) is further tested. Overall, RIM is capable to reproduce the observed IW-induced NRCS contrasts and their dependence on IW wavelength, wind speed and direction. Accordingly, RIM is suggested to be a robust tool to analyze near-nadir SWOT NRCS data. RIM is used to estimate sea surface MSS contrasts, and thus NRCS SWOT ones, caused by IWs over a wide range of wind conditions and IW wavelengths. In different wind speeds, maximum MSS contrasts occur when IWs propagate in the wind direction. This condition provides resonance between surface and internal waves, leading to the appearance of periodic zones with strong enhancement - suppression of surface roughness.

The implications of these investigations extend beyond the Amazon shelf. IWs play a vital role in ocean mixing, energy transfer, and nutrient transport, all crucial for understanding broader oceanographic and climatic processes. Resolving IW characteristics with unprecedented details, SWOT demonstrates its capability to advance our knowledge of these phenomena, particularly in regions where in-situ measurements are limited. Moreover, lessons gained from SWOT can enhance the RIM formulation, enabling a more quantitative interpretation of optical and traditional off-nadir synthetic aperture radar (SAR) observations, as well as future bi-static NRCS and Doppler measurements from the ESA EE10 Harmony SAR mission.

Data Availability

The data supporting reported results are extracted as following: SWOT Unsmoothed L2 and L3 CalVal data `https://aviso-data-center.cnes.fr/` (accessed on 25 July 2024); Multi Observation Global Ocean 3D Temperature Salinity Height Geostrophic Current and MLD `https://data.marine.copernicus.eu/` (accessed 15 April 2024); Gibbs Sea Water (GSW) oceanographic toolbox `https://www.teos-10.org/` (accessed 26 April 2024).

Acknowledgments

The work under this project was supported by the Ministry of Science and Higher Education of Russia, State assignment 0763-2020-0005 and FSZU-2025-0005. B.C. is supported by the ERC project 856408-STUOD and ESA Contract No. 4000135827/21/NL-Harmony Science Data Utilization and Impact Study for Ocean.

Appendix A IW Description: Three-Layer Stratification Approximation

The governing equation describing IW dynamics in the stratified ocean reads (Gill, 1982)

$$\frac{\partial^2 \hat{W}}{\partial z^2} + K^2 \frac{N^2 - \Omega^2}{\Omega^2} \hat{W} = 0, \tag{A1}$$

where $\hat{W}(z)$ is the Fourier amplitude of the vertical velocity, which is a function of z. K and Ω are IW wavenumber and frequency, $N(z)$ is the Brunt-Väisälä frequency. In Equation A1, we assumed that the IW frequency significantly exceeds the inertial frequency: $\Omega >> f$. In the tree-layer approximation of ocean stratification, introduced in Section 3.1, the Brunt-Väisälä frequencies in seasonal and the main pycnoclines are constant and equal to N_1 and N_2, respectively). For the abyssal pycnocline, $N_3 = 0$.

The general solution of Equation A1 in each of the layers reads:

$$\hat{W}_j(z) = A_{1j} \exp\left(iK \frac{\sqrt{N_j^2 - \Omega^2}}{\Omega} z \right) + A_{2j} \exp\left(-iK \frac{\sqrt{N_j^2 - \Omega^2}}{\Omega} z \right). \tag{A2}$$

where the index “j” refers to the layer number in the three-layer approximation, and A_{1j} and A_{2j} are constants that should be defined. The boundary conditions ensure continuity of vertical velocity and its derivative across the layer interfaces as well as zeroing of $\hat{W}$ on the surface and on the bottom are:

$$\begin{array}{ll} \hat{W}_1 = 0, & \text{at } z = 0 \\ \hat{W}_1 = \hat{W}_2 \text{ and } \partial \hat{W}_1/\partial z = \partial \hat{W}_2/\partial z, & \text{at } z = d_1 \\ \hat{W}_2 = \hat{W}_3 \text{ and } \partial \hat{W}_2/\partial z = \partial \hat{W}_3/\partial z, & \text{at } z = d_2 \\ \hat{W}_3 = 0, & \text{at } z = H \end{array} . \tag{A3}$$

where d_1 and d_2 are the depths of the lower boundary of the seasonal and the main pycnoclines respectively, H is the bottom depth.

First, we define profile of vertical velocity which corresponds to SSHA observed by SWOT. Relationship between the Fourier component of SSHA and gradient of vertical velocity amplitude at $z = 0$ is given by Equation 2, which can be rewritten as

$$\frac{\partial \hat{W}_1}{\partial z} = -i\frac{g\Omega}{C^2}\hat{h}(K) \tag{A4}$$

In order to reconstruct IW-induced undulations of the ocean layers which are manifested on the ocean surface as the surface height anomalies detectable by SWOT, Equation A4 should be taken into account together with boundary conditions Equation A3. Then the general solution A2 being applied to the boundary conditions A3 and A4 results in the following profile of vertical velocity in three-layer stratified ocean:

$$\frac{\hat{W}_1}{A} = \sin\left(\mu_1 K z\right). \tag{A5}$$

$$\frac{\hat{W}_2}{A} = \begin{cases} w_0 \sinh\big(K\mu_{22}(z-d_1)+\varphi_1\big), & \text{if } \Omega^2 \geq N_2^2, \\ w_0 \sin\big(K\mu_{21}(z-d_1)+\varphi_2\big), & \text{if } \Omega^2 < N_2^2. \end{cases} \tag{A6}$$

$$\hat{W}_3 = \hat{W}_2(d_2)\frac{\sinh\left[K\left(H-z\right)\right]}{\sinh\left[K\left(H-d_2\right)\right]} \tag{A7}$$

where A is a scale of vertical velocity related to SSHA via Equation A4 and equal to

$$A = -i\frac{g}{C}\frac{\Omega}{\sqrt{N_1^2-\Omega^2}}\hat{h}. \tag{A8}$$

$\mu_1^2 = (N_1^2 - \Omega^2)/\Omega$, $\mu_{21}^2 = (N_2^2 - \Omega^2)/\Omega$, and $\mu_{22}^2 = (\Omega^2 - N_2^2)/\Omega^2$, w_0 is dimensionless amplitude of vertical velocity:

$$w_0 = \begin{cases} \left[-\sin^2(K\mu_1 d_1) + \left(\frac{\mu_1}{\mu_{22}}\right)^2\cos^2(K\mu_1 d_1)\right]^{1/2} & \text{if } \Omega^2 \geq N_2^2, \\ \left[\sin^2(K\mu_1 d_1) + \left(\frac{\mu_1}{\mu_{21}}\right)^2\cos^2(K\mu_1 d_1)\right]^{1/2} & \text{if } \Omega^2 < N_2^2. \end{cases} \tag{A9}$$

and phases φ_1 and φ_2 are defined as:

$$\tanh\varphi_1 = (\mu_{22}/\mu_1)\tan\left(K\mu_1 d_1\right), \tag{A10}$$

$$\tan\varphi_2 = (\mu_{21}/\mu_1)\tan\left(K\mu_1 d_1\right), \tag{A11}$$

The dispersion equation for IWs, connecting Ω and K, is found by substituting the general solution A2 into the boundary conditions A3, resulting in a system of six algebraic equations. A nontrivial solution to this system of equations exists when the determinant of the system is equal to zero, which gives the dispersion relation for IWs. Omitting simple algebraic transformations, the final expression for the dispersion relation reads:

$$\begin{array}{ll} \sin\left(K\mu_1 d_1 + \varphi_3\right) = 0, & \text{if } \Omega^2 \geq N_2^2, \\ \sin\left(K\mu_1 d_1 + \varphi_4\right) = 0, & \text{if } \Omega^2 < N_2^2, \end{array} \tag{A12}$$

so, as a result for the nth mode of IWs, we get to

$$\begin{array}{ll} K\mu_1 d_1 + \varphi_3 = n\pi, & \text{if } \Omega^2 \geq N_2^2, \\ K\mu_1 d_1 + \varphi_4 = n\pi, & \text{if } \Omega^2 < N_2^2. \end{array} \tag{A13}$$

In Equations A5–A13, φ_3 and φ_4, are respectively as following:

$$\tan\varphi_3 = (\mu_1/\mu_{22})\tanh\left[K\mu_{22}\left(d_2 - d_1\right) + \varphi\right], \tag{A14}$$

$$\tan\varphi_4 = (\mu_1/\mu_{21})\tan\left[K\mu_{21}\left(d_2 - d_1\right) + \varphi\right], \tag{A15}$$

where, φ is defined as

$$\begin{cases} \tanh\varphi = \mu_{22}\tanh\left[K\left(H - d_2\right)\right], & \text{if } \Omega^2 \geq N_2^2, \\ \tan\varphi = \mu_{21}\tanh\left[K\left(H - d_2\right)\right], & \text{if } \Omega^2 < N_2^2. \end{cases} \tag{A16}$$

Solutions (A5) – (A7) for vertical velocity, and (A13) for dispersion relation, provide, a three-layered approximation model, describing the vertical motions caused by the IWs in the stratified ocean, which is used in the analysis described in Sections 3.2 and 4.

References

Bai, X., Lamb, K. G., & da Silva, J. C. B. (2021). Small-scale topographic effects on the generation of along-shelf propagating internal solitary waves on the amazon shelf. *Journal of Geophysical Research: Oceans*, *126*(8), e2021JC017252. Retrieved from `https://agupubs.onlinelibrary.wiley.com/doi/abs/10.1029/2021JC017252` (e2021JC017252 2021JC017252) doi: https://doi.org/10.1029/2021JC017252

Brandt, P., Rubino, A., & Fischer, J. (2002). Large-amplitude internal solitary waves in the north equatorial countercurrent. *Journal of Physical Oceanography*, *32*(5), 1567 - 1573. doi: 10.1175/1520-0485(2002)032⟨1567:LAISWI⟩2.0.CO;2

Cai, T., Zhao, Z., D'Asaro, E., Wang, J., & Fu, L.-L. (2024). Internal tide variability off central california: Multiple sources, seasonality, and eddying background. *Journal of Geophysical Research: Oceans*, *129*(8), e2024JC020892. Retrieved from `https://agupubs.onlinelibrary.wiley.com/doi/abs/10.1029/2024JC020892` (e2024JC020892 2024JC020892) doi: https://doi.org/10.1029/2024JC020892

Cox, C., & Munk, W. (1954, November). Measurement of the roughness of the sea surface from photographs of the sun's glitter. *Journal of the Optical Society of America*, *44*(11), 838. Retrieved from `http://dx.doi.org/10.1364/JOSA.44.000838` doi: 10.1364/josa.44.000838

de Macedo, C. R., Koch-Larrouy, A., da Silva, J. C. B., Magalhães, J. M., Lentini, C. A. D., Tran, T. K., ... Vantrepotte, V. (2023). Spatial and temporal variability in mode-1 and mode-2 internal solitary waves from modis-terra sun glint off the amazon shelf. *Ocean Science*, *19*(5), 1357–1374. Retrieved from `https://os.copernicus.org/articles/19/1357/2023/` doi: 10.5194/os-19-1357-2023

Dong, D., Yang, X., Li, X., & Li, Z. (2016). Sar observation of eddy-induced mode-2 internal solitary waves in the south china sea. *IEEE Transactions on Geoscience and Remote Sensing*, *54*(11), 6674-6686. doi: 10.1109/TGRS.2016.2587752

Fu, L.-L., Pavelsky, T., Cretaux, J.-F., Morrow, R., Farrar, J. T., Vaze, P., ... Dibarboure, G. (2024). The surface water and ocean topography mission: A breakthrough in radar remote sensing of the ocean and land surface water. *Geophysical Research Letters*, *51*(4), e2023GL107652. Retrieved from `https://agupubs.onlinelibrary.wiley.com/doi/abs/10.1029/2023GL107652` (e2023GL107652 2023GL107652) doi: https://doi.org/10.1029/2023GL107652

Gerkema, T. (1996). A unified model for the generation and fission of internal tides in a rotating ocean. *Journal of Marine Research*, *54*(3), 421–450.

Gill, A. E. (1982). *Atmosphere—ocean dynamics.* Academic Press.
Jackson, C. (2007). Internal wave detection using the moderate resolution imaging spectroradiometer (modis). *Journal of Geophysical Research: Oceans*, *112*(C11). Retrieved from https://agupubs.onlinelibrary.wiley.com/doi/abs/10.1029/2007JC004220 doi: https://doi.org/10.1029/2007JC004220
Johannessen, J. A., Kudryavtsev, V., Akimov, D., Eldevik, T., Winther, N., & Chapron, B. (2005). On radar imaging of current features: 2. mesoscale eddy and current front detection. *Journal of Geophysical Research: Oceans*, *110*(C7). Retrieved from https://agupubs.onlinelibrary.wiley.com/doi/abs/10.1029/2004JC002802 doi: https://doi.org/10.1029/2004JC002802
Kudryavtsev, V., Akimov, D., Johannessen, J., & Chapron, B. (2005). On radar imaging of current features: 1. model and comparison with observations. *Journal of Geophysical Research: Oceans*, *110*(C7). Retrieved from https://agupubs.onlinelibrary.wiley.com/doi/abs/10.1029/2004JC002505 doi: https://doi.org/10.1029/2004JC002505
Kudryavtsev, V., Monzikova, A., Combot, C., Chapron, B., & Reul, N. (2019). A simplified model for the baroclinic and barotropic ocean response to moving tropical cyclones: 2. model and simulations. *Journal of Geophysical Research: Oceans*, *124*(5), 3462-3485. Retrieved from https://agupubs.onlinelibrary.wiley.com/doi/abs/10.1029/2018JC014747 doi: https://doi.org/10.1029/2018JC014747
Kudryavtsev, V., Monzikova, A., Combot, C., Chapron, B., Reul, N., & Quilfen, Y. (2019). A simplified model for the baroclinic and barotropic ocean response to moving tropical cyclones: 1. satellite observations. *Journal of Geophysical Research: Oceans*, *124*(5), 3446-3461. Retrieved from https://agupubs.onlinelibrary.wiley.com/doi/abs/10.1029/2018JC014746 doi: https://doi.org/10.1029/2018JC014746
Kudryavtsev, V., Myasoedov, A., Chapron, B., Johannessen, J. A., & Collard, F. (2012). Imaging mesoscale upper ocean dynamics using synthetic aperture radar and optical data. *Journal of Geophysical Research: Oceans*, *117*(C4). Retrieved from https://agupubs.onlinelibrary.wiley.com/doi/abs/10.1029/2011JC007492 doi: https://doi.org/10.1029/2011JC007492
Lentini, C. A., Magalhães, J. M., da Silva, J. C., & Lorenzzetti, J. A. (2016, December). Transcritical flow and generation of internal solitary waves off the amazon river: Synthetic aperture radar observations and interpretation. *Oceanography*. Retrieved from https://doi.org/10.5670/oceanog.2016.88
Li, X., Jackson, C. R., & Pichel, W. G. (2013). Internal solitary wave refraction at dongsha atoll, south china sea. *Geophysical Research Letters*, *40*(12), 3128-3132. doi: https://doi.org/10.1002/grl.50614
Li, X., Zhao, Z., & Pichel, W. G. (2008). Internal solitary waves in the northwestern south china sea inferred from satellite images. *Geophysical Research Letters*, *35*(13). doi: https://doi.org/10.1029/2008GL034272
Magalhães, J., Alpers, W., Santos-Ferreira, A., & da Silva, J. (2021, June). Surface wave breaking caused by internal solitary waves: Effects on radar backscattering measured by sar and radar altimeter. *Oceanography*, *34*(2). Retrieved from http://dx.doi.org/10.5670/oceanog.2021.203 doi: 10.5670/oceanog.2021.203
Magalhães, J. M., & Da Silva, J. C. B. (2018). Internal solitary waves in the andaman sea: New insights from sar imagery. *Remote Sensing*, *10*(6). Retrieved from https://www.mdpi.com/2072-4292/10/6/861 doi: 10.3390/rs10060861
Magalhães, J. M., da Silva, J. C. B., Buijsman, M. C., & Garcia, C. A. E. (2016). Effect of the north equatorial counter current on the generation and propagation of internal solitary waves off the amazon shelf (sar observations). *Ocean Science*, *12*(1), 243–255. Retrieved from https://os.copernicus.org/articles/12/243/2016/ doi: 10.5194/os-12-243-2016

Morrow, R., Fu, L.-L., Ardhuin, F., Benkiran, M., Chapron, B., Cosme, E., ... Zaron, E. D. (2019). Global observations of fine-scale ocean surface topography with the surface water and ocean topography (swot) mission. *Frontiers in Marine Science*, *6*. Retrieved from https://www.frontiersin.org/journals/marine-science/articles/10.3389/fmars.2019.00232 doi: 10.3389/fmars.2019.00232

Moum, J., Farmer, D., Smyth, W., Armi, L., & Vagle, S. (2003). Structure and generation of turbulence at interfaces strained by internal solitary waves propagating shoreward over the continental shelf. *Journal of Physical Oceanography*, *33*(10), 2093–2112.

New, A. (1988). Internal tidal mixing in the bay of biscay. *Deep Sea Research Part A. Oceanographic Research Papers*, *35*(5), 691-709. Retrieved from https://www.sciencedirect.com/science/article/pii/019801498890026X doi: https://doi.org/10.1016/0198-0149(88)90026-X

Pingree, R., Mardell, G., & New, A. (1986). Propagation of internal tides from the upper slopes of the bay of biscay. *Nature*, *321*(6066), 154–158.

Qiu, B., Chen, S., Wang, J., & Fu, L.-L. (2024). Seasonal and fortnight variations in internal solitary waves in the indonesian seas from the swot measurements. *Journal of Geophysical Research: Oceans*, *129*(7), e2024JC021086. Retrieved from https://agupubs.onlinelibrary.wiley.com/doi/abs/10.1029/2024JC021086 (e2024JC021086 2024JC021086) doi: https://doi.org/10.1029/2024JC021086

Shaw, P.-T., Ko, D. S., & Chao, S.-Y. (2009). Internal solitary waves induced by flow over a ridge: With applications to the northern south china sea. *Journal of Geophysical Research: Oceans*, *114*(C2).

Shroyer, E. L., Moum, J. N., & Nash, J. D. (2010). Vertical heat flux and lateral mass transport in nonlinear internal waves. *Geophysical Research Letters*, *37*(8). Retrieved from https://agupubs.onlinelibrary.wiley.com/doi/abs/10.1029/2010GL042715 doi: https://doi.org/10.1029/2010GL042715

SWOT Project. (2023). *Swot level-2 karin low rate ssh unsmoothed.* CNES. Retrieved from https://www.aviso.altimetry.fr/en/data/products/sea-surface-height-products/global/swot-karin-low-rate-ocean-products.html doi: 10.24400/527896/A01-2023.016

Tchilibou, M., Carrere, L., Lyard, F., Ubelmann, C., Dibarboure, G., Zaron, E. D., & Arbic, B. K. (2024). Internal tides off the amazon shelf in the western tropical atlantic: Analysis of swot cal/val mission data. *EGUsphere*, *2024*, 1–23. Retrieved from https://egusphere.copernicus.org/preprints/2024/egusphere-2024-1857/ doi: 10.5194/egusphere-2024-1857

Tchilibou, M., Koch-Larrouy, A., Barbot, S., Lyard, F., Morel, Y., Jouanno, J., & Morrow, R. (2022). Internal tides off the amazon shelf during two contrasted seasons: interactions with background circulation and ssh imprints. *Ocean Science*, *18*(6), 1591–1618. Retrieved from https://os.copernicus.org/articles/18/1591/2022/ doi: 10.5194/os-18-1591-2022

Thomson, R. E., & Emery, W. J. (2014). Chapter 5 - time series analysis methods. In R. E. Thomson & W. J. Emery (Eds.), *Data analysis methods in physical oceanography (third edition)* (Third Edition ed., p. 425-591). Boston: Elsevier. Retrieved from https://www.sciencedirect.com/science/article/pii/B9780123877826000053 doi: https://doi.org/10.1016/B978-0-12-387782-6.00005-3

Valenzuela, G. R. (1978). Theories for the interaction of electromagnetic and oceanic waves—a review. *Boundary-Layer Meteorology*, *13*(1), 61–85.

Voronovich, A. G., & Zavorotny, V. U. (2001). Theoretical model for scattering of radar signals in k u - and c-bands from a rough sea surface with breaking waves. *Waves in Random Media*, *11*(3), 247–269. Retrieved from https://doi.org/10.1080/13616670109409784 doi: 10.1080/13616670109409784

Welch, P. (1967). The use of fast fourier transform for the estimation of power spectra: A method based on time averaging over short, modified periodograms. *IEEE Transactions on Audio and Electroacoustics*, *15*(2), 70-73. doi: 10.1109/TAU.1967.1161901

Xudong, Z., Xiaofeng, L., & Tao, Z. (2020, September). Characteristics and generations of internal wave in the sulu sea inferred from optical satellite images. *Journal of Oceanology and Limnology*, *38*(5), 1435-1444. Retrieved from http://dx.doi.org/10.1007/s00343-020-0046-1 doi: 10.1007/s00343-020-0046-1

Zhang, H., Fan, C., Sun, L., & Meng, J. (2024, May). Study of the ability of swot to detect sea surface height changes caused by internal solitary waves. *Acta Oceanologica Sinica*, *43*(5), 54–64. Retrieved from http://dx.doi.org/10.1007/s13131-024-2324-9 doi: 10.1007/s13131-024-2324-9

Zhang, M., Wang, J., Chen, X., Mei, Y., & Zhang, X. (2019). An experimental study on the characteristic pattern of internal solitary waves in optical remote-sensing images. *International Journal of Remote Sensing*, *40*(18), 7017–7032. Retrieved from https://doi.org/10.1080/01431161.2019.1597308 doi: 10.1080/01431161.2019.1597308

Zhang, X., & Li, X. (2024, April). Unveiling three-dimensional sea surface signatures caused by internal solitary waves: insights from the surface water ocean topography mission. *Journal of Oceanology and Limnology*, *42*(3), 709–714. Retrieved from http://dx.doi.org/10.1007/s00343-024-3286-7 doi: 10.1007/s00343-024-3286-7